

# Rhombohedral ( $R\bar{3}$ ) Prussian White as cathode material: An ab-initio study

Sebastian Baumgart,<sup>†</sup> Mohsen Sotoudeh,<sup>†</sup> and Axel Groß<sup>\*,†,‡</sup>

<sup>†</sup>*Institute of Theoretical Chemistry, Ulm University, Oberberghof 7, 89081 Ulm, Germany*

<sup>‡</sup>*Helmholtz Institute Ulm (HIU) for Electrochemical Energy Storage, Helmholtzstraße 11, 89081 Ulm, Germany*

E-mail: axel.gross@uni-ulm.de

## Abstract

Prussian whites (PW) have gained attention for their potential application as high energy density cathodes in Na-ion batteries. However, the rhombohedral phase of this compound still remains elusive. This study addresses the electronic and structural properties of the rhombohedral host material, as well as its ionic conductivity. Using periodic density functional theory calculations, we identified the critical factors that determine the sodium ion site preference and their ionic mobility. Specifically, the significant role of octahedral tilting and trigonal distortions of the structure have been highlighted. The study shows that the competition between coordination and bond length governs the Na site preference in the rhombohedral phase upon distortion. The results furthermore suggest that the redox activity is dominated by the transition metals. These findings provide valuable insights into the fundamental mechanisms underlying ionic conductivity in solid hosts and could thus help enhance ion transport in battery electrodes.

# Introduction

The renewable energy sector constantly requires new and inventive grid storage solutions to meet the growing demand. It is particularly important to handle the strain on the electrical grid caused by the diurnal shift from peak energy production to peak energy demand.<sup>1</sup> Although lithium-ion technology is currently the most advanced battery technology, it has significant drawbacks, including high cost, material supply risks, and low sustainability.<sup>2</sup>

These drawbacks have directed significant attention towards alternative battery technologies in the scientific community today.<sup>3-5</sup> Among these alternatives, the most promising one currently is the sodium ion battery (SIB),<sup>6,7</sup> which is chemically similar to lithium ion batteries. While commercial SIB products are beginning to emerge and are announced to be utilized in even electric vehicles, they have yet to match the performance of lithium ion batteries in terms of gravimetric or volumetric energy density. Nonetheless, the main driving force behind the development of high-performance sodium ion batteries is the desire to avoid escalating costs and supply risks associated with the limited availability of resources.<sup>6</sup> As a result, sodium ion battery development is primarily focused on applications in large-scale grid storage, where sacrificing energy density for lower costs or longer battery life is more acceptable. Since the discovery of hard carbon (nongraphitizable carbon) as a suitable anode material for sodium ion insertion,<sup>8</sup> the cathode material has become the bottleneck of SIB development.<sup>9</sup>

In this regard, materials based on Prussian blue (PB,  $A_{0.2}Fe[Fe(CN)_6]$ ) and their analogues (PBA,  $A_{0.2}B[B'(CN)_6]$ ) are a highly suitable cathode candidate for a sustainable grid storage solution utilizing SIBs. These materials offer a combination of long cycle life, high rate capability, and abundant elements, resulting in low material costs and no supply risk, even in the long run.<sup>10-12</sup> This advantage is particularly prominent in the historically longest-known Prussian blue variant,<sup>13,14</sup> where iron atoms occupy both transition metal (TM) sites.

Initially, Prussian blue based materials were known as a non-stoichiometric, cubic ( $Fm\bar{3}m$ )

double-perovskite compound with a lattice constant of 10.16 Å and a high content of coordinated and interstitial water within its crystal defects.<sup>15</sup> The significant amount of 25 % Fe<sup>3+</sup> vacancies was later found to be the very reason for the poor performance as a battery material measured in these early studies.<sup>16-18</sup> Recently though, compounds with a high sodium content (low vacancy content) have emerged which could live up to the expectations that were initially placed upon Prussian blue as a battery material.<sup>19-21</sup> These materials are often called Prussian white (PW) after the white color they exhibit when freshly synthesized in the fully sodiated state. They have been revealed to be a distorted, rhombohedral ( $R\bar{3}$ ) phase with lattice constants of  $a=b=6.5$  Å,  $c=18.9$  Å.<sup>19</sup> While being an object of intense research focus for some time, these compounds are still not fully studied theoretically. Therefore, to better understand the performance of Prussian white during a charge-discharge cycle, we shall explore its basic electronic configuration.

## Basic electronic configuration

The  $d$ -orbitals of any transition metal (TM) within an isotropic environment (e.g. a spherical field) are degenerate. The energy they exhibit in this situation is often called the barycenter, which in non-spherical situations is derived as the average energy of the  $d$ -orbitals.

According to ligand field theory,<sup>22</sup> which itself evolved out of crystal field theory,<sup>23,24</sup> the presence of the ligands within the (perfect) octahedral crystal environment present in the cubic variant of Prussian blue based materials lifts the degeneracy of the  $d$ -orbitals. The  $d_{xy}$ ,  $d_{xz}$  and  $d_{yz}$  orbitals, collectively called  $t_{2g}$  states after Mulliken,<sup>25</sup> are lowered in energy with respect to the barycenter, while the  $d_{x^2}$  and  $d_{z^2-y^2}$  orbitals (or  $e_g$  states) increase their energy. The amount of energy the orbitals are separated by is called the crystal field splitting energy (CFSE), which is dependent on the ligand environment around the TM. This energy is distributed in such a way that the energy of the barycenter still exactly coincides with the energy of the degenerate  $d$ -orbitals.<sup>26</sup> While empty or fully filled shells of electrons do not gain energy via this splitting, it can be energetically beneficial for partially filled shells.

As mentioned above the ligand environment dictates the size of the crystal field splitting energy. Some of the most common ligands are collected and ordered according to their ligand strength within the spectrochemical series of ligands first proposed in 1938.<sup>27,28</sup> From this series the ligands that are typical electron donors like the halides or hydroxide cause the CFSE to decrease, while electron acceptor ligands like carbonmonoxide increase the CFSE. The splitting can be further de-/increased by ligands that exhibit strong  $\pi$ -bonding or  $\pi$ -backbonding, respectively. This is especially relevant for transition metal complexes with 4-7 electrons within their  $d$ -orbitals, because the size of their CFSE relative to the spin pairing energy (SPE) determines whether a high spin (hs) or low spin (ls) complex is formed.<sup>22</sup> The first three electrons introduced into an octahedrally coordinated TM will always be placed separately into the three  $t_{2g}$  states. If the CFSE is small compared to the energy necessary for pairing electrons within one state, it is more beneficial to start filling the  $e_g$  states with single electrons before pairing electrons within one orbital. The result is a high spin configuration. Conversely, if the CFSE is large in relation to the SPE, it would minimize the energy to place the fourth electron into one of the  $t_{2g}$  states, paying the price for pairing the electrons rather than gaining less by placing it into a higher orbital, resulting in a low spin configuration.

Transitioning to the distorted octahedral environment encountered in the rhombohedral ( $R\bar{3}$ ) PB variant. Due to Prussian blue being a double perovskite type material and octahedral tilting in Perovskites being extensively studied, it is known that a phase of this symmetry has to be formed by a cooperative out-of-phase rotation of the  $\text{FeC}_6$  and  $\text{FeN}_6$  octahedra in all three directions of space ( $a^-a^-a^-$  rotation after Glazer).<sup>29-34</sup> Such a rotation often causes the trigonal distortion,<sup>35,36</sup> which further splits the  $d$ -orbitals by forming one  $a_{1g}$  and two  $e'_g$  states out of the already favourable  $t_{2g}$ -states. The  $a_{1g}$  state is further lowered in energy in comparison to both the barycenter and the  $t_{2g}$ -states. The  $e'_g$  states therefore have to increase in energy compared to the  $t_{2g}$ -states, but they still will be lower than the overall barycenter energy.

In an actual, fully sodiated Prussian blue based system (e.g.  $\text{Na}_2\text{Fe}[\text{Fe}(\text{CN})_6]$ ), both Fe atoms are in the +2 oxidation state. Nevertheless, they are distinguishable because of the differences in their chemical (ligand) environment. The iron coordinated to the carbon atom of the cyanide ligand experiences a strong field due to the carbon site of the cyanide ligand being a strong  $\pi$ -acceptor. This causes a large splitting of the  $d$ -orbitals, which results in a low spin configuration of the carbon-coordinated Fe atoms. Contrary, the iron atoms that are coordinated to the nitrogen are exposed to an effective  $\pi$ -donor, wherefore they experience a weak field and stabilize in a high spin configuration. While the splitting of the  $d$ -orbitals for the high spin Fe is only slightly beneficial in energy, there is a large energy gain due to all electrons of the low spin Fe being lowered in an octahedral crystal environment. Furthermore, it can be seen in Figure 1 that such a material benefits not only from the  $t_{2g}/e_g$  splitting within an octahedral field, but increases the energy gain on the high spin Fe atoms upon formation of the  $a_{1g}/e'_g$  states, benefiting the phase transition seen in experiment.

Upon desodiation, the rhombohedral phase gradually changes back into the cubic one.<sup>21</sup> It seems that desodiation causes local changes in the crystal system that only then propagate through the material until one sodium equivalent per formula unit is removed. Simultaneously, one of the paired electrons in the  $a_{1g}$  orbital of the high spin Fe atoms is removed. This leads to the splitting of the  $t_{2g}$  states being energy neutral, while the splitting of the  $d$ -states experienced in an octahedral field still stays beneficial with respect to the barycenter due to the energy gained on the low spin Fe atoms. At this point the material corresponds to the well-known cubic Prussian blue structure ( $\text{NaFe}[\text{Fe}(\text{CN})_6]$ ).

Further desodiation now leads to the so-called Prussian Yellow ( $\text{Fe}[\text{Fe}(\text{CN})_6]$ ) and the removal of one of the electrons out of the  $t_{2g}$  states of the low spin Fe. This does obviously not erase the benefits of the  $t_{2g}/e_g$  splitting. If anything, it actually gives rise to a small energy benefit by the formation of the  $a_{1g}/e'_g$  states. This energy gain would suggest a small driving force towards a rhombohedral crystal system, which is not known from the experiment. Therefore, we shall seek to explore reasons as to why the rhombohedral structure is observed

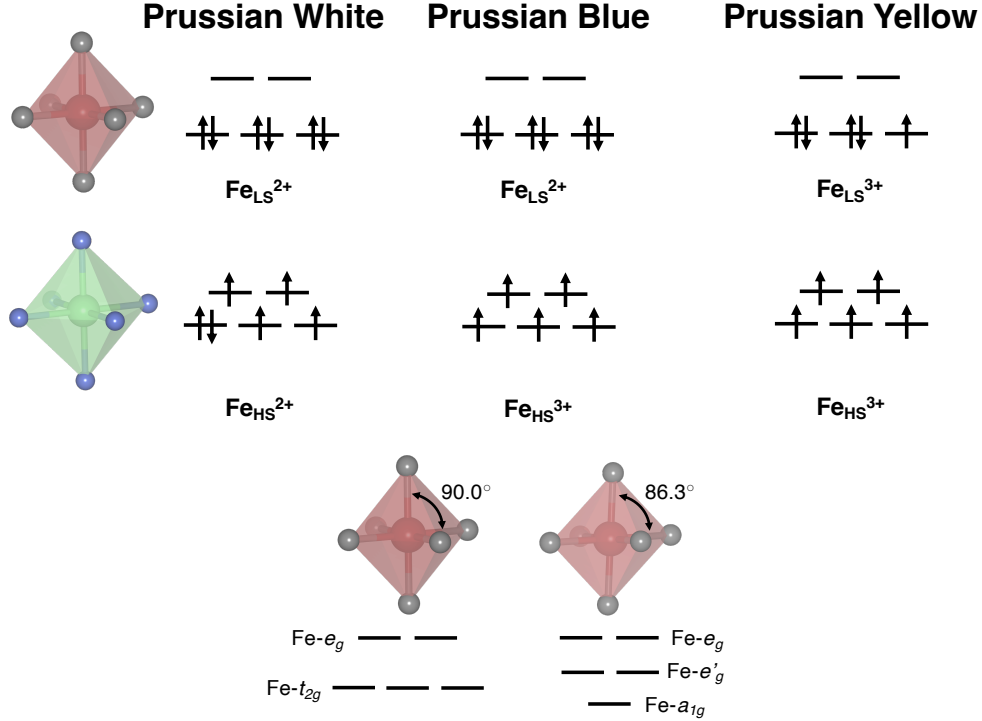


Figure 1: Schematic picture depicting the splitting of the high spin and low spin Fe- $d$  states in different crystal environments. The bottom figure illustrates the transition from an undistorted octahedron cage ( $O_h$  octahedral symmetry) to a trigonally distorted cage ( $D_{3h}$  octahedral symmetry) and the associated further crystal field splitting of the Fe- $d$  states.

for Prussian White only from the standpoint of atomistic first-principles calculations.

In this paper, we further report the theoretical description of the structural and electronic properties of the high performance, rhombohedral Prussian white (R-PW) system. We observe a significant influence of ion concentration on the stability of Na preferred sites, which we attribute to the distortion and corresponding changes in lattice constants. By considering the geometry, we identify the interatomic distances in the face centered sites as an indicator of cation stability within the PB lattice. Furthermore, we demonstrate that the lattice distortion causes a migration away from the face cubic centered plane into the vertexes of the cubes during the phase transition. These results on R-PW shall be put into perspective by comparison with the cubic phase of Prussian white (C-PW), as well as with available experimental data. Additionally, we present first-principles electronic structure calculations to investigate the mobility of Na-ions in PB structures. Our focus is specifically

on understanding the electronic properties that govern ion migration in these materials.

## Computational Details

Density functional theory (DFT)<sup>37-39</sup> calculations were performed using version 6.2.1 of the Vienna *Ab-initio* Simulation Package (VASP),<sup>40,41</sup> employing the plane-wave method. The projector augmented wave (PAW) approach<sup>41,42</sup> was utilized to replace the inner electrons. The generalized gradient approximation (GGA) proposed by Perdew, Burke, and Ernzerhof<sup>43</sup> was chosen as the exchange-correlation functional. To address the known issue of overdelocalization associated with GGA functionals, the Hubbard  $U$ -correction was applied to the iron  $d$ -states, as suggested by Dudarev et al.<sup>44</sup> Previous studies<sup>45</sup> have indicated that the structural and electronic properties of Prussian white are best represented by applying distinct  $U$ -values to the two iron sites. Therefore, a Hubbard correction of 7 eV was assigned to the  $d$ -states of high-spin  $\text{Fe}^{2+}$ , while a value of 3 eV was used for the  $d$ -states of low-spin  $\text{Fe}^{2+}$ . To ensure convergence to the correct high-spin-low-spin spin state, the total excess majority spin electrons were held constant. The plane-wave cutoff was set to 550 eV, and a Gaussian smearing method with a width of 0.1 eV was employed. A gamma-centered k-point grid of  $5 \times 5 \times 3$  was employed to sample the Brillouin zone. The atomic structures underwent optimization until the energy difference in the electronic self-consistent field (SCF) fell below  $10^{-6}$  eV, and all forces were less than  $10^{-2}$  eV/Å. The initial structure containing three formula units and exhibiting  $R\bar{3}$  symmetry was adapted from the structural parameters published by Wang et al.<sup>21</sup>

The NEB calculations<sup>46,47</sup> have been carried out using the PBE functional with four distinct images in a charge-neutral fashion to evaluate the Na-ion migration minimum energy path. An extended discussion as to why the Hubbard  $U$ -correction was dropped for the NEB calculations can be found in the SI in the section "Supplementary Discussion: The failure of GGA+U". To allow for migration in Prussian White, one charge carrier atom was removed

from the fully sodiated cell. The reported structure was determined to be sufficiently large to ensure a negligible interaction between the periodic images of the migrating sodium ions. All structures were fully relaxed until the forces on the atoms were converged within  $10^{-2}$  eV/Å.

## Results and Discussion

### Crystal structure

The crystal structure of Prussian white follows a double-perovskite structure represented by the general chemical formula  $A_{0.2}Fe[Fe(CN)_6]$ . In this structure, the oxide ions of a typical perovskite structure are replaced by  $(C\equiv N)^-$  anions. The empty grid, devoid of alkali metal cations, has recently been called Prussian Yellow, while the half filled structure is named Prussian Blue and the fully filled structure is called Prussian White. Additionally, different transition metals like manganese, nickel, cobalt, zinc, copper, chromium, vanadium, and titanium can replace iron in the crystal structure without disrupting it. These variations form a group of compounds called Prussian-blue analogues, which share similar chemical compositions and crystal structures. The defect-free Prussian-blue framework typically adopts a face-centered cubic structure with large spaces between atoms that can accommodate cations and water molecules. Transition-metal ions coordinated with carbon prefer a low-spin configuration due to the strong crystal field, while nitrogen-coordinated transition-metal ions favor a high-spin configuration due to the weaker crystal field. The rapid formation of Prussian blue in water solutions often involves the incorporation of vacancies, and transition metal ions near these vacancies tend to coordinate with water molecules, leading to a lattice distortion. This distortion can affect the activation energy required for the diffusion of guest cations within the framework's interstitial space. Moreover, the presence of coordinated water molecules and the insertion of guest cations can induce structural distortions and reduce the symmetry of Prussian-blue compounds from their primary cubic structure to monoclinic, rhombohedral, or tetragonal structures. Among these, Prussian-blue materials with a rhom-

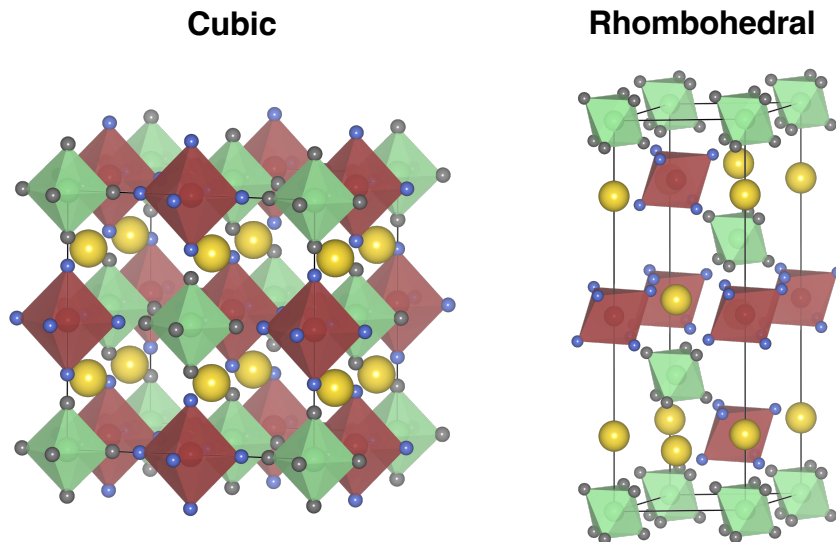


Figure 2: The Prussian White material with its cubic and rhombohedral crystal structures. In these structures, the high-spin transition-metal ion is represented by a red sphere, the low-spin transition-metal ion is represented by a green sphere. Coordination polyhedra were made slightly transparent, colored in accordance with the color of their central atom. The nitrogen atoms are represented by a blue sphere, the carbon atoms by a grey sphere, and the sodium atoms by a yellow sphere.

bohedral structure and low content of coordinated water are particularly advantageous as cathodes in rechargeable batteries.<sup>20</sup>

The optimized crystal structure of rhombohedral Prussian White (R-PW) exhibits the  $R\bar{3}$  symmetry as shown in Figure 2, with the octahedral coordination of the high spin and low spin  $\text{Fe}^{+2}$  still being the dominant feature. The cooperative out-of-phase rotation of the octahedra still allows for straight  $\text{C}\equiv\text{N}$  bonds after the distortion. The rotation is accompanied by a shift of the sodium atoms along the  $[111]$  axis of the cubic cell towards its vertices leading to a concentration of the sodium atoms within "layers" (along the  $c$ -axis) of  $\text{FeN}_6$  octahedra. This in turn optimizes the Na-N interactions in the crystal, providing an octahedral coordination of nitrogen around the sodium atoms. Within these Na-N octahedra the sodium ions move towards the face site which is not face-connected to an  $\text{FeC}_6$  octahedra as to optimize the space available to them.

Alternatively, one can imagine that the  $c$ -axis of the rhombohedral cell coincides with

the [111] axis of the cubic cell. The image of a cube standing on its vertex alone would intuitively describe the occurrence of the 3-fold rhombohedral symmetry that is inherited from the cubic system and the manifestation of alternating  $\text{FeC}_6$  and  $\text{FeN}_6$  octahedra layers. Completing this image, one may now imagine that in the vertex of this cube there is a sodium ion, which would be surrounded by three  $\text{FeN}_6$  octahedra, while the cation is closed in by one  $\text{FeC}_6$  octahedra either above or below. This sodium ion would therefore shift away from this already allocated site towards the void, optimizing its neighbor interactions in the process. Additional images visually representing both transformations can be found in Figure S1.

The conventional cell of pristine, cubic Prussian White (C-PW) is depicted in Figure 2 for comparison. It shows the octahedra of high spin and low spin Fe atoms being perfectly aligned along the Fe-CN-Fe bonds, which in itself are aligned perfectly along the crystal axis. As already reported by other theoretical works,<sup>48,49</sup> it seems that in the cubic phase sodium will prefer to sit within the face centered interstitial site (Wyckoff position 24d) instead of occupying the body centered void (Wyckoff position 8c). The exact energetic behaviour of this phenomenon and an extended structural comparison can be found in Figure S2 and Table S1. Interestingly, the above presented structural changes in R-PW lead to the structure of the face centered interstitial site being stretched in one direction, while being compressed in the other. This change significantly reduces the space available to the sodium ion by 30%, causing a migration away from the fcc plane into the vertices of the cubes during the phase transition. The full account of these geometric factors can be found in Figure S3 and Table S2. We tried to also energetically compare the equivalents of the interstitial positions known from the cubic phase with their equivalents in R-PW, but these positions are - despite extensive efforts - not stable enough to converge within our set convergence criteria. Instead, after the optimization process the sodium ions always revert back to their minimum energy positions.

A comparison of the calculated structural properties between the cubic and rhombohedral phases of PW, as well as experimental data for two rhombohedral PW compounds is

Table 1: Structural properties of rhombohedral Prussian White (R-PW,  $\text{Na}_2\text{Fe}[\text{Fe}(\text{CN})_6]$ ) in comparison with experimental values. Additionally given are experimental values for the isomorphous  $\text{Na}_2\text{Mn}[\text{Fe}(\text{CN})_6]$  (NaMnHCF) and calculated values for the cubic phase of Prussian white (C-PW,  $\text{Na}_2\text{Fe}[\text{Fe}(\text{CN})_6]$ ).

Property	C-PW	<b>R-PW</b>	Exp. <sup>19</sup>	NaMnHCF <sup>20</sup>
Space group	Fm $\bar{3}$ m (225)	R $\bar{3}$ (148)	R $\bar{3}$ (148)	R $\bar{3}$ (148)
a, b [ $\text{\AA}$ ]	10.498	6.480	6.548	6.580
c [ $\text{\AA}$ ]	–	19.364	18.931	18.929
V [ $\text{\AA}^3$ ]	1156.96	704.05	702.96	709.75
d( $\text{Fe}_{\text{ls}}^{2+}$ -C) [ $\text{\AA}$ ]	1.878	1.886	–	1.896*
d(C-N) [ $\text{\AA}$ ]	1.181	1.183	–	1.173*
d( $\text{Fe}_{\text{hs}}^{2+}$ -N) [ $\text{\AA}$ ]	2.190	2.186	–	2.246*
d( $\text{Fe}_{\text{ls}}^{2+}$ - $\text{Fe}_{\text{hs}}^{2+}$ ) [ $\text{\AA}$ ]	5.249	4.941	–	4.938
$\alpha$ ( $\text{Fe}_{\text{ls}}^{2+}$ -C-N) [ $^\circ$ ]	180	171.9	–	175
$\alpha$ ( $\text{Fe}_{\text{hs}}^{2+}$ -N-C) [ $^\circ$ ]	180	141.9	–	140
$\alpha$ (C- $\text{Fe}_{\text{ls}}^{2+}$ -C) [ $^\circ$ ]	90	93.6 / 86.4	–	91.7 / 88.3*
$\alpha$ (N- $\text{Fe}_{\text{hs}}^{2+}$ -N) [ $^\circ$ ]	90	88.8 / 91.8	–	88.0 / 92.0*

\*Value obtained by evaluating the published Rietveld refinement parameters on data obtained by TOF powder neutron diffraction.

presented in Table 1. Although the isomorphous compound NaMnHCF - or more accurately  $\text{Na}_2\text{Mn}[\text{Fe}(\text{CN})_6]$  - listed in the last column differs in the TM that is occupying the high spin B-sites in the material, there are strong indications that the TM used to build the stable Prussian blue framework does not influence its structure much.<sup>34</sup> This can be verified by our calculations as well as by comparison with both experimental sources. The advantage of taking this PBA material into account lay in the published Rietveld refinement data, that allow for a more in-depth comparison of structural features, which are not available for the pure compound.

The calculated lattice constant for the rhombohedral Prussian white match within 2.5% to the experimental values. Even more accurately described are the volume of the system and all measured distances, on average deviating by less than one percent. The volume (per formula unit) of the unit cell is decreased from  $289.2 \text{ \AA}^3$  to  $234.7 \text{ \AA}^3$  during the cubic to rhombohedral phase transformation. As described in the Introduction, this reduction of the cell volume by almost 20% is accompanied by a displacement of the cyanide ligands.

This displacement has to be an angular shift of the cyanide ligands with respect to the Fe-CN-Fe axis, as it causes a shortening of the Fe-Fe distance, while keeping all other distances constant. The fact that the observed bond angles are deviating from their ideal values verifies this conclusion. Due to the strong  $\pi$ -backbonding interactions that dominate the Fe-cyanide interactions, linear Fe-C bonds are favoured and the carbon atoms are found to show a lower mobility compared to the nitrogen end of the ligand.<sup>34,50</sup> This is expressed by the larger deviation from the ideal  $180^\circ$  angle in  $\alpha(\text{Fe}_{\text{ls}}^{2+}\text{-C-N})$  as compared to  $\alpha(\text{Fe}_{\text{hs}}^{2+}\text{-N-C})$ . These calculated angular values are in great agreement with the experimental data.<sup>19</sup>

Lastly, we find a change in the bond angles within the Fe octahedra, which shows that the  $\text{FeC}_6$  and  $\text{FeN}_6$  octahedra are not only rotated, but also slightly deformed with respect to the cubic crystal environment. Ideally, these angles should all amount to  $90^\circ$ , but in the rhombohedral phase the octahedra are slightly distorted. While the  $\text{FeC}_6$  octahedra are stretched in the direction of the  $c$ -axis, the  $\text{FeN}_6$  octahedra are getting compressed, which leads to inverse trends in the change of bond angles of these octahedra. The C-Fe-C angles within one layer perpendicular to the  $c$ -axis are narrowed, while the angles between carbons in different layers are increased and exactly the other way around for the angles between iron and nitrogen. The change is more pronounced for the Fe carbons angles, but even there does not exceed  $4^\circ$  total. We propose that these changes are caused by the presence of intercalated sodium ions. Due to the proximity of the sodium atoms the negatively charged nitrogens bend towards them, stretching the  $\text{FeN}_6$  octahedra in the  $a/b$  plane. This directly results in a compression of the octahedra in the  $c$ -direction, which is partly compensated by the stretching of the  $\text{Fe-C}_6$  octahedra. This change in the ligand field around the Fe atoms is also the reason for the further splitting of the  $t_{2g}$  states into  $a_{1g}/e'_g$  states being energetically beneficial, as described in the Introduction. These structural changes are verified to actually occur in this material by the experimental data on  $\text{NaMnHCF}$ .<sup>19</sup>

The argumentation that the sodium atoms themselves are the cause for the rhombohedral transformation would also directly solve the dilemma of why no rhombohedral phase exists

for Prussian Yellow. As this compound does not contain any sodium ions, which would be there to cause the distortions and stabilize the rhombohedral structure, this phase is never thermodynamically favorable. To confirm this assumption we calculated the empty rhombohedral phase and compared it to its cubic counterpart. It can be shown that the Prussian Yellow structure is not thermodynamically stable in  $R\bar{3}$  symmetry, as it is destabilized by 0.62 eV per formula unit over the cubic one.

## Evaluation of electronic properties

The calculated DOS of R-PW is shown in Figure 3 (top). The filled valence band, which extends from -9 to 0 eV, is predominantly of N-2*p* character (red), C-2*p* character (orange) mixed with Fe-3*d* orbitals (blue). They represent the Fe-N, Fe-C, and N-C bonding states. The empty Fe-*d* states are located 2-5 eV above the valence band. The octahedral crystal-field splitting divides the Fe-*d* states into  $\pi$ -bonding  $t_{2g}$  states (green), and  $\sigma$ -bonding  $e_g$  states (yellow) as shown in the bottom graph of Figure 3. The states around the Fermi energy are dominated by the Fe-*d* states, showing that the redox activity is dominated by the iron atoms. Especially noteworthy is the only partially filled, narrow band of minority spin states, which lies directly on top of the Fermi energy. These are the  $a_{1g}$ -states newly filled in the transition from Prussian blue to Prussian White, causing a transition from the semiconducting to conducting behavior. Furthermore, a small contribution of carbon *p*-states can be observed, which hints at the strong  $\pi$ -bonding interactions present in this material class.<sup>51-54</sup> The DOS of cubic Prussian white is similar to the rhombohedral crystal structure except for the shift in the Fermi energy and consequently the occupation of the minority  $a_{1g}$ -states (the calculated DOS of C-PW is provided in the supplementary information in Figure S4).

To further analyze the contributions to the DOS of rhombohedral Prussian white, the orbital-decomposed DOSs of the Fe-*d* states for high-spin and low-spin Fe are presented in Figure 4. The states around the Fermi level of high spin Fe are dominated by contributions

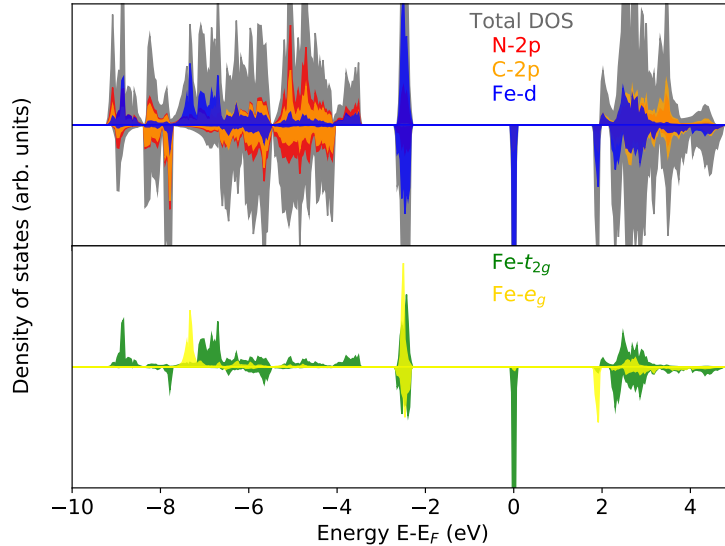


Figure 3: The calculated electronic density of states (DOS) for the rhombohedral Prussian White phase. The total DOS is given in grey in the top graph. The projected DOS are shown in blue for Fe- $d$  states, in red for N- $2p$  states, and in orange for C- $2p$  states. The Fermi energy is shifted to 0 eV. The majority spin states are plotted upwards, while the minority spin states are plotted downwards. The bottom graph shows the orbital decomposed Fe- $d$  states, namely  $t_{2g}$  (green) and  $e_g$  (yellow) orbitals.

of the minority spin direction. All majority spin states shift down in energy, therefore being far from the Fermi level. All states shown from -6 eV to 0 eV do not contain contributions from high spin Fe either. Conversely, it can be observed that the state lying on the Fermi energy is purely constructed from the high spin Fe orbitals. They can be attributed to the  $a_{1g}$ -states formed during the rhombohedral phase transition. Also visible are the still unoccupied  $e'_g$ -states at around 1.8 eV above the Fermi energy. The minority spin  $e_g$ -states are again shifted out of frame, this time to values higher than 6 eV.

For the plot concerning the low-spin iron, the splitting of the states is much clearer compared to the high-spin iron. This is one cluster of states around -2 eV that represent the  $a_{1g}/e'_g$ -states of low-spin iron and a second cluster of states starting at +2 eV that can be ascribed to the  $e_g$ -states. Due to these states being either completely filled or empty, no shift between the majority and minority spin states can be observed.

Finally, in Table 2 we compare some electronic properties. As already seen in the pre-

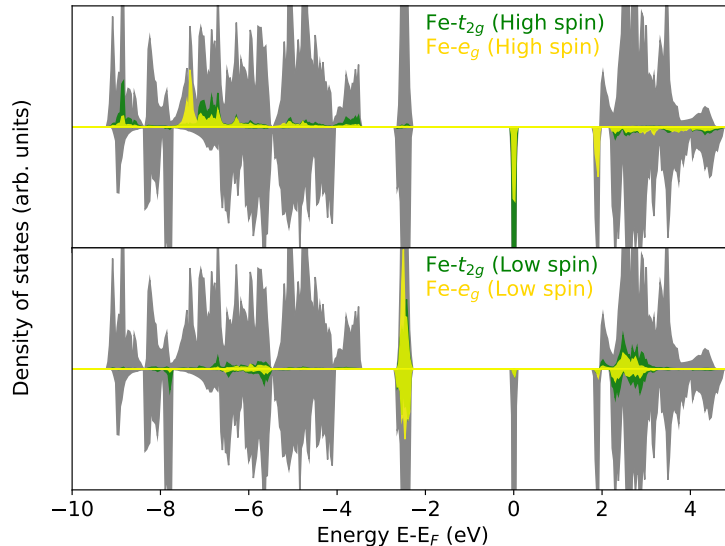


Figure 4: Orbital decomposed DOS of the Fe- $d$  states. The top graph depicts the DOS for the high-spin Fe centers, while the states for the low-spin Fe centers are depicted on the bottom graph. The energy zero is set to the top of the valence band and Fe- $t_{2g}$  and Fe- $e_g$  orbitals are given in green and yellow, respectively.

Table 2: Electronic properties of rhombohedral Prussian White ( $\text{Na}_2\text{Fe}[\text{Fe}(\text{CN})_6]$ ).

Property	C-PW	<b>R-PW</b>	experimental
$\Delta E_g$ [eV]	cond.	cond.	cond. <sup>55</sup>
$\mu_{\text{Fe(II)-C}}$ [ $\mu_B$ ]	0.022	0.054	0*
$\mu_{\text{Fe(II)-N}}$ [ $\mu_B$ ]	3.652	3.711	4*

\* Formal number of unpaired electrons

vious paragraph, the calculations for both, cubic and rhombohedral Prussian white, are in accordance with the experiment on PW being a conductor. We also address the magnetization of both iron species for cubic and rhombohedral PW. Both phases are showing a clear distinction between the irons, matching the experimentally seen high-spin-low-spin configuration. Furthermore, the total amount of magnetization matches the formally expected values within the expected error margins.

## Migration barriers

The minimum energy path for the sodium migration in the low vacancy limit is illustrated in Figure 5. The high vacancy limit is not studied as the  $R\bar{3}$  phase only persists in the

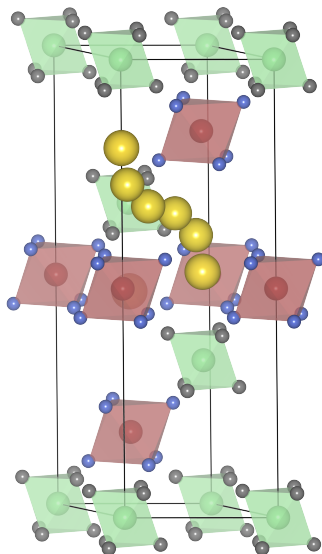


Figure 5: Depiction of the studied NEB path within rhombohedral Prussian White. High- and low-spin iron is shown in red and green, respectively. Carbon is shown in grey, nitrogen in blue, and sodium in yellow. Non-migrating sodium atoms are not shown for improved clarity.

material as long as a high sodium content is present. Otherwise the material reverts back to its cubic phase. The removal of one sodium ion from the unit cell results in a material with the formula  $\text{Na}_{1.66}\text{Fe}[\text{Fe}(\text{CN})_6]$ .

The migration path that is studied in R-PW still remains similar to the diffusion pathways and transition states seen in cubic PW. Sodium ions are placed in a vertex of one of the small cubic structures (cubes) within a unit cell of R-PW, migrating to one of the neighboring cubes. Due to the distortions that occur by forming the rhombohedral phase, these cubes are slightly distorted, but the general structural feature persists. The transition state for this diffusion corresponds to the face-centered site, which is spanned by a square of Fe-CN-Fe units on each of the square edges. Due to the shift of the sodium atoms into the vertices of the cubes, there is one position that is close to the connecting/separating face-centered plane and one farther into the small cubic structure. Here, we particularly studied the migration, where a sodium ion is starting from a place far from the separating plane to an equal place on the other side, as illustrated in Figure 5. A comparative analysis of both phases reveals that

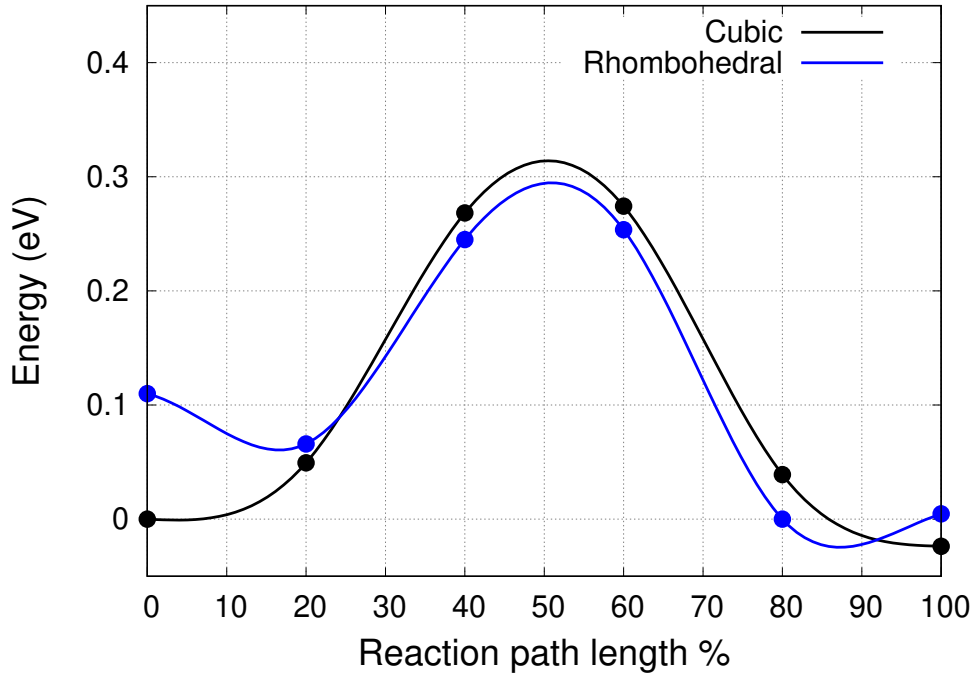
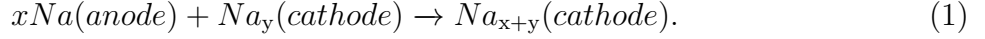


Figure 6: Na migration energy barriers (in eV) as a function of the reaction path coordinate derived from periodic DFT calculations combined with NEB for the single-ion migration from the initial site to the next nearest neighboring site corresponding to the  $\text{Na}_2\text{Fe}[\text{Fe}(\text{CN})_6]$  PW with the cubic crystal structure (black color) and with rhombohedral crystal structure (blue color). The minimum energy is set to zero.

$\text{Na}^+$  diffusion in the cubic phase exhibits a reduced energy barrier, as depicted in Figure 6. The stability of face-centered sites in the C-PW framework, devoid of distortions, ensures a uniform distribution of  $\text{Na}^+$  in three dimensions and lowers the activation energy through cooperative migrations. The presence of a low diffusion barrier significantly facilitates rapid  $\text{Na}^+$  migration, thus directly influencing the rate performance of SIB cathode materials. However, both phases exhibit fast  $\text{Na}^+$  diffusion, highlighting their importance.

## Voltages upon cation intercalation

Finally, we discuss a critical factor influencing the efficiency of a battery, namely the open-circuit voltage. The voltage of a battery results from the gain in the free energy  $\Delta G$  upon the overall chemical reaction



As the alkali metal atoms are still combined with their electrons (within the electron sea) in the metal anode and are recombined with an electron upon intercalation into the cathode, the overall reaction can be expressed in terms of atoms. The open circuit voltage ( $V_{OC}$ ) is defined as the maximum voltage  $V$  of the battery.<sup>39,56</sup> It can be expressed as

$$V_{OC} = \frac{-\Delta G}{xF}. \quad (2)$$

Here,  $x$  is the charge transferred during the above given chemical reaction and  $F$  is the Faraday constant. The open circuit voltage can equivalently be expressed in terms of the difference in chemical potential of the anode  $\mu_A$  and cathode  $\mu_C$ .

$$V_{OC} = [\mu_A - \mu_C]/e \quad (3)$$

This voltage can be approximated utilizing total system energies that are easily obtained by DFT calculations. Note that typically metallic anodes are taken as a reference to derive the open circuit voltage of cathode materials. In this case equation 3 can be rewritten as

$$V_{OC} = -\frac{[E_{x_1} - E_{x_2} - (x_1 - x_2)E_{\text{metal}}]}{n(x_1 - x_2)e}. \quad (4)$$

Here,  $E_{x_1}$  and  $E_{x_2}$  correspond to the energy of the system before and after intercalation. Similarly,  $x_1$  and  $x_2$  denote the number of charge carriers present in the respective unit cell.  $E_{\text{metal}}$  is the energy of the metal system and  $n$  is the transferred charge between anode and cathode during one iteration of the above described chemical reaction. For a single transfer of a simple, monovalent charge carrier the equation is reduced significantly.

$$V_{OC} = -[E_{x_1} - E_{x_2} - E_{\text{metal}}]/e \quad (5)$$

Using equation 5, we compare the voltages for the intercalation of sodium at a high sodium content in the cubic and rhombohedral phases. Due to differences in the unit cell size, in the case of the rhombohedral phase, the voltage calculation concerns the range from  $\text{Na}_{1.66}\text{Fe}[\text{Fe}(\text{CN})_6]$  to  $\text{Na}_2\text{Fe}[\text{Fe}(\text{CN})_6]$ , while the cubic phase is calculated for the reaction from  $\text{Na}_{1.75}\text{Fe}[\text{Fe}(\text{CN})_6]$  to  $\text{Na}_2\text{Fe}[\text{Fe}(\text{CN})_6]$ . The results for these calculations are summarized in Table 3.

Table 3: Open circuit voltage for the last insertion step in rhombohedral and cubic Prussian White.

Property	C-PW	R-PW	Experiment <sup>20,21</sup>
Voltage [V]	2.77	2.50	2.8 - 3.3

The intercalation potentials for the last sodium insertion step in rhombohedral and cubic Prussian White were calculated to be at 2.5 V and 2.77 V, respectively. These results agree reasonably well with the experiment but slightly underestimate measured open circuit voltages, which becomes apparent when comparing with experimental values of 2.8-3.3 V. Note, however, that open circuit voltages depend on the state of charge of batteries, i.e., on the concentration of the charge carriers in the electrode materials, and deviations between theory and experiments might be caused by differences in these concentrations. Overall, as is characteristic for SIBs, the voltages are comparatively lower than those of lithium compounds, which operate at intercalation voltages of 4 to 5 V.

## Conclusion

In this study, we have investigated the structural and electronic properties of Prussian White crystal structures together with their properties as battery cathode materials for Na-ion batteries, in particular Na ion mobility and open circuit voltage, using periodic density functional theory calculations. Our findings indicate that the transition metals dominate the redox-active site upon Na insertion into the host lattice, with the two Prussian Whites considered exhibiting low diffusion barriers of approximately 0.3 eV. Furthermore, our calculations

highlight the crucial role of octahedral tilting and trigonal distortion in the rhombohedral structure, influencing the preferred Na site. Though increasing Na content leads to trigonal distortions and results in slightly larger migration barriers and decreased diffusivities, the impact of the distortion on these barriers is smaller than previously expected. Moreover, these materials exhibit open-circuit potentials of around 2.8 V for the cubic structure and 2.5 V for the rhombohedral structure, relative to metallic Na. These characteristics position them as promising cathode materials for SIBs. Our calculations provide a comprehensive understanding of the internal mechanism involved in the transportation of  $\text{Na}^+$  within the PW frameworks. Overall, our results, along with the analysis of electronic and geometric factors, provide a conceptual framework for comprehending ionic conductivity in Prussian White electrode materials. This framework can be applied to enhance our understanding and improve ion mobility in other material classes as well.

## Acknowledgement

This work contributes to the research performed at CELEST (Center for Electrochemical Energy Storage Ulm-Karlsruhe) and was funded by the German Research Foundation (DFG) under Project ID 390874152 (POLiS Cluster of Excellence). The authors acknowledge support by the state of Baden-Württemberg through bwHPC and the German Research Foundation (DFG) through grant no INST 40/575-1 FUGG (JUSTUS 2 cluster).

## References

- (1) Rahman, M. A.; Kim, J.-H.; Hossain, S. Recent advances of energy storage technologies for grid: A comprehensive review. *Energy Storage* **2022**, *4*, e322.
- (2) Schmuch, R.; Wagner, R.; Hörpel, G.; Placke, T.; Winter, M. Performance and cost

- of materials for lithium-based rechargeable automotive batteries. *Nat. Energy* **2018**, *3*, 267–278.
- (3) Armand, M.; Tarascon, J.-M. Building better batteries. *Nature* **2008**, *451*, 652–657.
- (4) Kim, H.; Kim, H.; Ding, Z.; Lee, M. H.; Lim, K.; Yoon, G.; Kang, K. Recent progress in electrode materials for sodium-ion batteries. *Adv. Energy Mater.* **2016**, *6*, 1600943.
- (5) Walter, M.; Kovalenko, M. V.; Kravchyk, K. V. Challenges and benefits of post-lithium-ion batteries. *New J. Chem.* **2020**, *44*, 1677–1683.
- (6) Usiskin, R.; Lu, Y.; Popovic, J.; Law, M.; Balaya, P.; Hu, Y.-S.; Maier, J. Fundamentals, status and promise of sodium-based batteries. *Nat. Rev. Mater.* **2021**, *6*, 1020–1035.
- (7) Gauckler, C.; Dillenz, M.; Maroni, F.; Pfeiffer, L. F.; Biskupek, J.; Sotoudeh, M.; Fu, Q.; Kaiser, U.; Dsoke, S.; Euchner, H.; Axmann, P.; Wohlfahrt-Mehrens, M.; Groß, A.; Marinaro, M. Detailed Structural and Electrochemical Comparison between High Potential Layered P2-NaMnNi and Doped P2-NaMnNiMg Oxides. *ACS Appl. Energy Mater.* **2022**, *5*, 13735–13750.
- (8) Euchner, H.; Vinayan, B. P.; Reddy, M. A.; Fichtner, M.; Groß, A. Alkali metal insertion into hard carbon – the full picture. *J. Mater. Chem. A* **2020**, *8*, 14205–14213.
- (9) Qian, J.; Wu, C.; Cao, Y.; Ma, Z.; Huang, Y.; Ai, X.; Yang, H. Prussian blue cathode materials for sodium-ion batteries and other ion batteries. *Adv. Energy Mater.* **2018**, *8*, 1702619.
- (10) Wu, X.; Deng, W.; Qian, J.; Cao, Y.; Ai, X.; Yang, H. Single-crystal FeFe (CN) 6 nanoparticles: a high capacity and high rate cathode for Na-ion batteries. *J. Mater. Chem. A* **2013**, *1*, 10130–10134.
- (11) Hurlbutt, K.; Wheeler, S.; Capone, I.; Pasta, M. Prussian blue analogs as battery materials. *Joule* **2018**, *2*, 1950–1960.

- (12) Yi, H.; Qin, R.; Ding, S.; Wang, Y.; Li, S.; Zhao, Q.; Pan, F. Structure and properties of prussian blue analogues in energy storage and conversion applications. *Adv. Funct. Mater.* **2021**, *31*, 2006970.
- (13) Woodward, J. Praeparatio Caerulei Prussiaci Ex Germania Missa ad Johannem Woodward, MD Prof. Med. Gresh. RSS. *Philos. Trans. R. Soc. Lond.* **1724**, *33*, 15–17.
- (14) Brown, J. V. Observation and experiments upon the foregoing preparation. *Philos. Trans. R. Soc. Lond.* **1724**, *33*, 17–24.
- (15) Ivanov, V. D. Four decades of electrochemical investigation of Prussian blue. *Ionics* **2020**, *26*, 531–547.
- (16) Jayalakshmi, M.; Scholz, F. Performance characteristics of zinc hexacyanoferrate/Prussian blue and copper hexacyanoferrate/Prussian blue solid state secondary cells. *J. Power Sources* **2000**, *91*, 217–223.
- (17) Kuwabara, K.; Nunome, J.; Sugiyama, K. Secondary Solid-State Cell: Copper/Prussian Blue. *J. Electrochem. Soc.* **1990**, *137*, 2001.
- (18) Kraft, A. Some considerations on the structure, composition, and properties of Prussian blue: a contribution to the current discussion. *Ionics* **2021**, *27*, 2289–2305.
- (19) Wang, L.; Song, J.; Qiao, R.; Wray, L. A.; Hossain, M. A.; Chuang, Y.-D.; Yang, W.; Lu, Y.; Evans, D.; Lee, J.-J., et al. Rhombohedral Prussian white as cathode for rechargeable sodium-ion batteries. *J. Am. Chem. Soc.* **2015**, *137*, 2548–2554.
- (20) Song, J.; Wang, L.; Lu, Y.; Liu, J.; Guo, B.; Xiao, P.; Lee, J.-J.; Yang, X.-Q.; Henkelman, G.; Goodenough, J. B. Removal of interstitial H<sub>2</sub>O in hexacyanometallates for a superior cathode of a sodium-ion battery. *J. Am. Chem. Soc.* **2015**, *137*, 2658–2664.
- (21) Wang, W.; Gang, Y.; Hu, Z.; Yan, Z.; Li, W.; Li, Y.; Gu, Q.-F.; Wang, Z.; Chou, S.-L.;

- Liu, H.-K., et al. Reversible structural evolution of sodium-rich rhombohedral Prussian blue for sodium-ion batteries. *Nat. Commun.* **2020**, *11*, 980.
- (22) Griffith, J.; Orgel, L. Ligand-field theory. *Quarterly Reviews, Chemical Society* **1957**, *11*, 381–393.
- (23) Bethe, H. Termaufspaltung in kristallen. *Ann. Phys.* **1929**, *395*, 133–208.
- (24) Van Vleck, J. Theory of the variations in paramagnetic anisotropy among different salts of the iron group. *Phys. Rev.* **1932**, *41*, 208.
- (25) Mulliken, R. S. Electronic structures of polyatomic molecules and valence. IV. Electronic states, quantum theory of the double bond. *Phys. Rev.* **1933**, *43*, 279.
- (26) Zuckerman, J. Crystal field splitting diagrams. *J. Chem. Educ.* **1965**, *42*, 315.
- (27) Tsuchida, R. Absorption spectra of co-ordination compounds. I. *Bull. Chem. Soc. Jpn.* **1938**, *13*, 388–400.
- (28) Shimura, Y.; Tsuchida, R. Absorption spectra of Co (III) complexes. II. Redetermination of the spectrochemical series. *Bull. Chem. Soc. Jpn.* **1956**, *29*, 311–316.
- (29) Glazer, A. M. The classification of tilted octahedra in perovskites. *Acta Crystallogr. B.* **1972**, *28*, 3384–3392.
- (30) Glazer, A. Simple ways of determining perovskite structures. *Acta Crystallogr. Sec. A: Crystal Physics, Diffraction, Theoretical and General Crystallography* **1975**, *31*, 756–762.
- (31) Howard, C. J.; Stokes, H. T. Group-theoretical analysis of octahedral tilting in perovskites. *Acta Crystallogr. B. Struct.* **1998**, *54*, 782–789.
- (32) Howard, C. J.; Stokes, H. T. Group-Theoretical Analysis of Octahedral Tilting in Perovskites. Erratum. *Acta Crystallogr. B. Struct.* **2002**, *58*, 565–565.

- (33) Howard, C. J.; Kennedy, B. J.; Woodward, P. M. Ordered double perovskites—a group-theoretical analysis. *Acta. Crystallogr. B. Struct.* **2003**, *59*, 463–471.
- (34) Boström, H. L.; Brant, W. R. Octahedral tilting in Prussian blue analogues. *J. Mater. Chem. C* **2022**, *10*, 13690–13699.
- (35) Sotoudeh, M.; Dillenz, M.; Groß, A. Mechanism of Magnesium Transport in Spinel Chalcogenides. *Adv. Energy Sustainability Res.* **2021**, *2*, 2100113.
- (36) Sotoudeh, M.; Dillenz, M.; Döhn, J.; Hansen, J.; Dsoke, S.; Groß, A. Oxide Spinel with Superior Mg Conductivity. *Chem. Mater.* **2023**, *35*, 4786–4797.
- (37) Hohenberg, P.; Kohn, W. Inhomogeneous Electron Gas. *Phys. Rev.* **1964**, *136*, B864–B871.
- (38) Kohn, W.; Sham, L. J. Self-Consistent Equations Including Exchange and Correlation Effects. *Phys. Rev.* **1965**, *140*, A1133–A1138.
- (39) Euchner, H.; Groß, A. Atomistic modeling of Li- and post-Li-ion batteries. *Phys. Rev. Materials* **2022**, *6*, 040302.
- (40) Kresse, G.; Furthmüller, J. Efficient iterative schemes for ab initio total-energy calculations using a plane-wave basis set. *Phys. Rev. B* **1996**, *54*, 11169.
- (41) Kresse, G.; Joubert, D. From ultrasoft pseudopotentials to the projector augmented-wave method. *Phys. Rev. B* **1999**, *59*, 1758.
- (42) Blöchl, P. E. Projector augmented-wave method. *Phys. Rev. B* **1994**, *50*, 17953.
- (43) Perdew, J. P.; Burke, K.; Ernzerhof, M. Generalized gradient approximation made simple. *Phys. Rev. Lett.* **1996**, *77*, 3865.

- (44) Dudarev, S. L.; Botton, G. A.; Savrasov, S. Y.; Humphreys, C.; Sutton, A. P. Electron-energy-loss spectra and the structural stability of nickel oxide: An LSDA+ U study. *Phys. Rev. B* **1998**, *57*, 1505.
- (45) Wojdeł, J. C.; de PR Moreira, I.; Bromley, S. T.; Illas, F. On the prediction of the crystal and electronic structure of mixed-valence materials by periodic density functional calculations: The case of Prussian Blue. *J. Chem. Phys.* **2008**, *128*, 044713.
- (46) Henkelman, G.; Jónsson, H. Improved tangent estimate in the nudged elastic band method for finding minimum energy paths and saddle points. *J. Chem. Phys.* **2000**, *113*, 9978–9985.
- (47) Henkelman, G.; Uberuaga, B. P.; Jónsson, H. A climbing image nudged elastic band method for finding saddle points and minimum energy paths. *J. Chem. Phys.* **2000**, *113*, 9901–9904.
- (48) Ling, C.; Chen, J.; Mizuno, F. First-principles study of alkali and alkaline earth ion intercalation in iron hexacyanoferrate: the important role of ionic radius. *J. Phys. Chem. C* **2013**, *117*, 21158–21165.
- (49) Hegner, F. S.; Galán-Mascarós, J. R.; López, N. A database of the structural and electronic properties of Prussian blue, Prussian white, and Berlin green compounds through density functional theory. *Inorg. Chem.* **2016**, *55*, 12851–12862.
- (50) Buser, H.; Schwarzenbach, D.; Petter, W.; Ludi, A. The crystal structure of Prussian blue: Fe<sub>4</sub> [Fe (CN) <sub>6</sub> ]<sub>3</sub> · 3xH<sub>2</sub>O. *Inorg. Chem.* **1977**, *16*, 2704–2710.
- (51) Tian, C.; Kan, E.; Lee, C.; Whangbo, M.-H.  $\pi$ -Back-Donation Effect of the Cyanide Ligands on the Electron Correlation and Charge Transfer in Prussian Blue RbMn [Fe (CN) <sub>6</sub> ]. *Inorg. Chem.* **2010**, *49*, 3086–3088.
- (52) Shriver, D. *Structure and bonding*; Springer, 2008; pp 32–58.

- (53) Kaim, W. “Guilty” Verdict—Evidence for the Noninnocence of Cyanide. *Angew. Chem. Int. Ed.* **2011**, *50*, 10498–10500.
- (54) Kettle, S. F. A.; Diana, E.; Boccaleri, E.; Stanghellini, P. L. The Vibrational Spectra of the Cyanide Ligand Revisited. *Bridging Cyanides*. 2007.
- (55) Xidis, A.; Neff, V. D. On the electronic conduction in dry thin films of Prussian blue, Prussian yellow, and Everitt’s salt. *J. Electrochem. Soc.* **1991**, *138*, 3637.
- (56) Groß, A.; Sakong, S. Modelling the electric double layer at electrode/electrolyte interfaces. *Curr. Opin. Electrochem.* **2019**, *14*, 1 – 6.